Selective methane oxidation by molecular iron catalysts in aqueous medium

https://doi.org/10.1038/s41586-023-05821-2

Received: 4 August 2022

Accepted: 10 February 2023

Published online: 5 April 2023

Check for updates

Hiroto Fujisaki[1], Tomoya Ishizuka[1], Hiroaki Kotani[1], Yoshihito Shiota[2], Kazunari Yoshizawa[2,3] & Takahiko Kojima[1,3] ✉

Using natural gas as chemical feedstock requires efficient oxidation of the constituent alkanes—and primarily methane[1,2]. The current industrial process uses steam reforming at high temperatures and pressures[3,4] to generate a gas mixture that is then further converted into products such as methanol. Molecular Pt catalysts[5–7] have also been used to convert methane to methanol[8], but their selectivity is generally low owing to overoxidation—the initial oxidation products tend to be easier to oxidize than methane itself. Here we show that *N*-heterocyclic carbene-ligated Fe^{II} complexes with a hydrophobic cavity capture hydrophobic methane substrate from an aqueous solution and, after oxidation by the Fe centre, release a hydrophilic methanol product back into the solution. We find that increasing the size of the hydrophobic cavities enhances this effect, giving a turnover number of 5.0×10^2 and a methanol selectivity of 83% during a 3-h methane oxidation reaction. If the transport limitations arising from the processing of methane in an aqueous medium can be overcome, this catch-and-release strategy provides an efficient and selective approach to using naturally abundant alkane resources.

Methane (CH_4) comprises approximately 90% of natural gas, which is a naturally abundant carbon resource[9,10]. Use of methane as a C1 raw material for the synthesis of value-added chemicals has therefore become increasingly important in the chemical industry[1,2]. The selective conversion of CH_4 to more-complex carbon-based compounds under mild conditions is one of the most important transformations both in nature[11–13] and for the chemical industry[3,4,14,15]. At present, the large-scale conversion of CH_4 to methanol (CH_3OH) is typically performed through steam reforming in conjunction with catalysis by CuO/ZnO/Al_2O_3 (refs. 3,4) and applying high pressures and temperatures. Therefore, the development of efficient and selective catalytic systems for CH_4 conversion that can be performed in aqueous media under mild conditions is considered a worthwhile goal related to sustainable development[1,2].

The selective conversion of CH_4 to CH_3OH is one of the most challenging oxidation reactions[1,2]. This is because the C–H bonds in CH_4 are highly inert, with a bond dissociation energy (BDE) of 105 kcal mol^{-1} (ref. 8), whereas the C–H bonds in CH_3OH are weak, with a BDE of 96 kcal mol^{-1} (ref. 16). Therefore, the latter is more reactive. Heterogeneous catalysts have also been reported to promote direct CH_4 oxidation to CH_3OH[2,17–21], but the conversion and selectivity obtained with these materials are not yet satisfactory[3,4]. In biological systems, metalloenzymes catalyse the conversion of CH_4 to CH_3OH under ambient conditions[11–13]. It has been proposed that during the hydroxylation of CH_4 by soluble methane mono-oxygenase (sMMO)[11], CH_4 reacts with the reactive bis(μ-oxo)diiron(IV) core in the hydrophobic cavity formed by the amino acid residues of the protein and is converted to hydrophilic CH_3OH, which is subsequently released to the surrounding aqueous medium[12,13].

Numerous metal complexes have been prepared to artificially catalyse the oxidation of CH_4 to CH_3OH and the reactivity of these materials has been examined[5,6,22–26]. For example, the CH_4 conversion to methyl bisulfate ($CH_3OS(O)_2OH$) with a selectivity of 81% using CH_4 at high pressure (9.0 MPa), H_2SO_4 as the oxidant and Pt complex as the catalyst was previously reported[6,7,14]. This process was expensive and also involved further steps to produce CH_3OH[5,6,14,15]. One of the most promising approaches to suppressing the overoxidation of CH_3OH during the catalytic oxidation of CH_4 is the use of catalysts with a substrate-trapping site or a hydrophobic cavity close to the catalytically active metal centre[8,11–13]. It would be beneficial to develop molecular oxidation catalysts enabling the efficient use of CH_4 as a naturally occurring feedstock. Here we report the highly efficient and selective catalysis of gaseous alkane oxidation using Fe^{II} complexes (acting as molecular catalysts) with hydrophobic second coordination spheres (SCSs) made of mesityl or anthracenyl substituents. On the basis of the proposed mechanism of selective oxidation by sMMO[13], we provide a concept for the design of catalysts with hydrophobic SCSs near the metal centre. These materials enable the selective and environmentally benign transformation of gaseous alkanes, including CH_4, as hydrophobic substrates in aqueous media through a so-called catch-and-release mechanism.

We synthesized Fe^{II} complexes of pentadentate ligands with one *N*-heterocyclic carbene (NHC) moiety bearing hydrophobic SCSs. These complexes had the general formula $[Fe(^{R}PY_4Cl_2BIm)(CH_3CN)](PF_6)_2$ (**2**-AN, R = mesityl (Mes); **3**-AN, R = anthracenyl (Ant); AN = CH_3CN) (Fig. 1a). The detailed synthetic protocols used to obtain **2**-AN and **3**-AN are provided in the Methods. Complex **1**-AN (R = H), without a hydrophobic SCS, was also synthesized for comparison purposes[27].

[1]Department of Chemistry, Faculty of Pure and Applied Sciences, University of Tsukuba, Tsukuba, Japan. [2]Institute for Materials Chemistry and Engineering, Kyushu University, Fukuoka, Japan. [3]CREST, Japan Science and Technology Agency (JST), Kawaguchi, Japan. ✉e-mail: kojima@chem.tsukuba.ac.jp

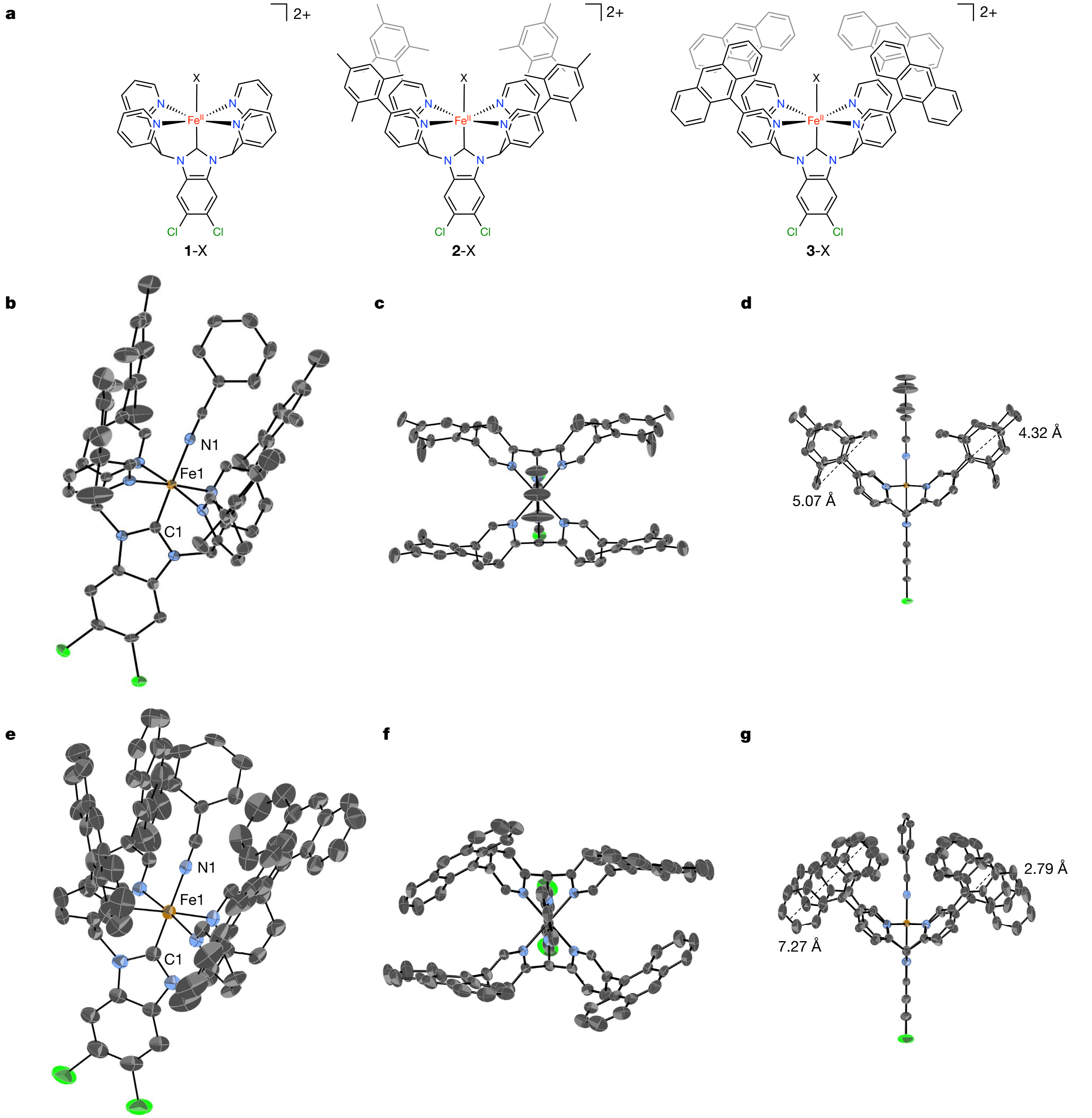

Fig. 1 | Structures of the Fe–NHC complexes used in this study. a, Schematic of **1**-X, **2**-X and **3**-X (X: OH_2, OD_2, $NCCH_3$ (= AN) or NCC_6H_5 (= BN)). **b**–**g**, ORTEP drawings of the cationic moieties of **2**-BN (**b**–**d**) and **3**-BN (**e**–**g**) were produced using 50% (**2**-BN) or 40% (**3**-BN) probability thermal ellipsoids: overall (**b**,**e**), top (**c**,**f**) and side (**d**,**g**) views. Hydrogen atoms and two PF_6^- ions have been omitted for clarity. Grey, carbon; blue, nitrogen; green, chlorine.

The low-spin Fe^{II}–NHC complexes **1**-AN, **2**-AN and **3**-AN were characterized by ^1H NMR spectroscopy (Supplementary Figs. 1–3) and electrospray ionization time-of-flight mass spectrometry (ESI-TOF-MS) (Supplementary Figs. 4–6). Fe^{II} complexes with benzonitrile (BN), **2**-BN (Fig. 1b–d) and **3**-BN (Fig. 1e–g), both of which contain a BN molecule as an axial ligand in place of AN, were also prepared to determine the crystal structures by X-ray crystallography (Supplementary Fig. 7 and Supplementary Table 1). The lengths of the Fe–C and Fe–N bonds determined were comparable, indicating that the electronic interactions in the first coordination sphere of each complex were almost identical.

We used *n*-butane, propane, ethane and methane as gaseous alkane substrates for catalytic oxidation. The oxidation was performed at 323 K under an atmosphere comprising one of the gaseous alkanes (butane, 0.1 MPa; propane, 0.7 MPa; ethane, 0.8 MPa; methane, 0.98 MPa) in a high-pressure glass tube containing a solution of **1**-AN, **2**-AN or **3**-AN (1.0 μM) as the precatalyst and sodium persulfate ($Na_2S_2O_8$, 5.0 mM) as the oxidant in D_2O:CD_3CN (95:5, v/v, 1.0 ml, pD (= −log[D^+]) was not adjusted). Under these conditions, the Fe^{II}–AN complexes used as precatalysts were converted to the corresponding Fe^{II}–OD_2 complexes **1**-OD_2, **2**-OD_2 and **3**-OD_2 through an exchange of the ligands (Supplementary Figs. 8–13).

Table 1 | Summary for the catalytic oxidations of gaseous alkanes

Substrates	BDE_{C-H} (kcal mol^{-1})	Products	Catalyst 1-OD_2 TON	1-OD_2 Total TON (Sel (%))	2-OD_2 TON	2-OD_2 Total TON (Sel (%))	3-OD_2 TON	3-OD_2 Total TON (Sel (%))
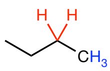 *n*-Butane (3.9 mM)	98.3 100.7	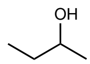	1.6×10^2	3.4×10^2 (48)	3.6×10^2	4.8×10^2 (75)	1.4×10^3	1.8×10^3 (78)
		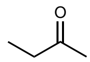	1.7×10^2		1.2×10^2		4.0×10^2	
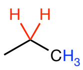 Propane (4.2 mM)	98.1 99.9	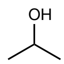	78	2.3×10^2 (34)	3.1×10^2	3.8×10^2 (83)	1.1×10^3	1.3×10^3 (88)
		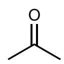	1.5×10^2		65		1.4×10^2	
C_2H_6 Ethane (4.7 mM)	100.5	C_2H_5OH	38	86 (44)	2.7×10^2	3.3×10^2 (83)	8.4×10^2	9.5×10^2 (89)
		CH_3COOH	48		58		1.1×10^2	
CH_4 Methane (3.5 mM)	105.0	CH_3OH	25	64 (38)	72	101 (71)	4.2×10^2	5.0×10^2 (83)
		HCOOH	39		29		83	

Conditions: [catalyst] = 1.0 μM, [$Na_2S_2O_8$] = 5.0 mM and T = 323 K. Reaction time = 3 h. BDE_{C-H} was obtained from a literature[16]. TONs were determined by ^{1}H NMR spectroscopy using sodium 3-(trimethylsilyl)propanesulfonate as an internal standard. TON = [product]/[catalyst]; total TON = [all products]/[catalyst]; Sel. indicates alcohol selectivity, calculated as 100×(TON of alcohol product)/total TON. Only by-products provided in the table were observed. CO_2 and O_2 were not observed in gas chromatography analyses of any reaction mixtures. HCHO was also not detected by the Nash colorimetric method[34] during the methane oxidation trials and CH_3CHO was not evident in the ^{1}H NMR spectra during the ethane oxidation trials. Very small amounts of the oxidation products were observed during reactions in the absence of catalysts or using Fe salts, such as $Fe(NO_3)_3$ and $Fe(ClO_4)_2$, as catalysts (Extended Data Table 1). For all substrates, the concentration of the respective gaseous alkane in the aqueous medium after passing through one of the gaseous alkanes is given.

Under the present conditions, the catalytic oxidation reactions afforded 2-butanol and 2-butanone from *n*-butane, 2-propanol and acetone from propane, ethanol and acetic acid from ethane, and methanol and formic acid from methane (Table 1 and Fig. 2). The catalytic turnover numbers (TONs) of the reactions when performed for 3 h were determined by ^{1}H NMR spectroscopy. We found that the TONs for the catalytic oxygenations of the four gaseous substrates using **3**-OD_2 as the catalyst were the largest among the three catalysts used (Table 1) and were much larger than those obtained from catalysis using iron salts (Extended Data Table 1). In the case of *n*-butane, propane and ethane oxidation by **3**-OD_2, highly selective two-electron oxidation (that is, hydroxylation) was found to afford the corresponding alcohols with TONs of 1.8×10^3, 1.3×10^3 and 9.5×10^2, respectively (Table 1 and Fig. 2). The associated selectivity values were 78% for 2-butanol, 88% for 2-propanol and 89% for ethanol. The total TON of 5.0×10^2 and the 83% CH_3OH selectivity obtained with the **3**-OD_2 during a 3-h CH_4 oxidation trial are some of the highest values reported for catalytic CH_4 oxidation using a molecular metal complex as the catalyst[22–26]. The 4.1% conversion of CH_4 and 83% CH_3OH selectivity by **3**-OD_2 at 323 K (see Methods) are higher than those of heterogeneous catalysts, such as metal-containing zeolite, which is active at 448–689 K (approximately 2% CH_4 conversion and around 58–82% CH_3OH selectivity)[2]. By contrast, we found that the oxidation of 2-propanol, ethanol and methanol using **3**-OD_2 as the catalyst had much smaller TONs for the corresponding oxidation products compared with those for the corresponding gaseous alkanes (Extended Data Table 2). These values were smaller than or comparable with the values observed without a catalyst. Thus, the oxidation of alcohols was predominantly attributed to the presence of $Na_2S_2O_8$. The TON obtained for the oxidation reactions of 2-propanol, ethanol and methanol was found to decrease in the order of **1**-OD_2 > **2**-OD_2 > **3**-OD_2 (Extended Data Table 2). These results indicate that the hydrophobic SCSs efficiently promoted oxidation of the hydrophobic substrates while hydrophilic oxidation products were rapidly released, thus suppressing overoxidation of these two-electron-oxidized products.

The gas chromatography–mass spectrometry analysis for the reaction mixture of the catalytic CH_4 oxidation using $Na_2S_2{}^{16}O_8$ in $H_2{}^{18}O:CH_3CN$ (95:5, v/v) indicated that only $CH_3{}^{18}OH$ was obtained and thus water acted as the sole oxygen source[27] (for the detection of $CH_3{}^{16}OH$, see Extended Data Fig. 1a,b and Supplementary Fig. 14). After a catalytic CH_4 oxidation reaction for 3 h using **3**-AN, the catalyst was found to be durable and 75% of the catalysts retained their original structure, as confirmed by ESI-TOF-MS, ultraviolet–visible (UV–vis) and ^{1}H NMR spectroscopy analyses (Supplementary Figs. 15–19).

The capture of CH_4 molecules in the hydrophobic SCSs of **3**-OD_2 was confirmed by titration experiments using ^{1}H NMR spectroscopy experiments in which **3**-OD_2 was added to solutions of CH_4 (0.05 mM) in $D_2O:CD_3CN$ (1:1, v/v) at 298 K. The ^{1}H NMR signal of CH_4 was observed at $\delta = 0.221$ ppm in the absence of **3**-OD_2. However, this signal was shifted upfield with increasing concentrations of **3**-OD_2 (Extended Data Fig. 2a). This phenomenon suggests that the CH_4 molecules were trapped in the hydrophobic SCSs of **3**-OD_2, probably because of CH–π interactions. Furthermore, the ^{1}H NMR signal of CH_4 was observed as one singlet peak, indicating a rapid exchange between free CH_4 molecules and those captured in the SCSs at 298 K (ref. 28). A nuclear Overhauser effect was observed between the hydrogen nuclei of CH_4 and those of anthracenyl moieties and at the 6-position of the pyridine moieties. This shows that the CH_4 molecules were located inside the hydrophobic cavities (Methods and Supplementary Figs. 20–31). Furthermore, the ^{1}H NMR signals derived from the Ant groups and NHC moieties of **3**-OD_2 also displayed moderate shifts after bubbling CH_4 through a solution of **3**-OD_2 in $D_2O:CD_3CN$ (1:1, v/v) at 298 K (Extended Data Fig. 2b).

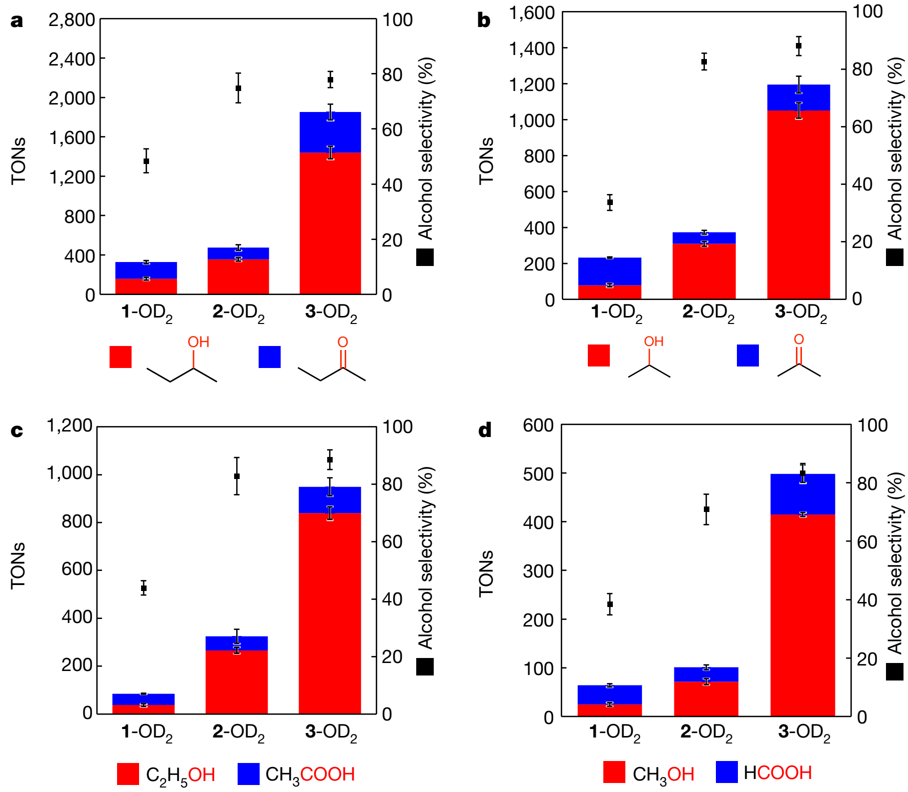

Fig. 2 | Comparison of TONs and alcohol selectivity among the three catalysts. **a**–**d**, Data for the oxidation of butane (**a**), propane (**b**), ethane (**c**) and methane (**d**). Red, TONs for the alcohol products (that is, two-electron-oxidized products); blue, TONs for the four-electron- or six-electron-oxidized products; black dots, alcohol selectivity (TONs for alcohol product/total TONs × 100, %). For reaction conditions, see Table 1. Data are mean ± s.d. from three experiments.

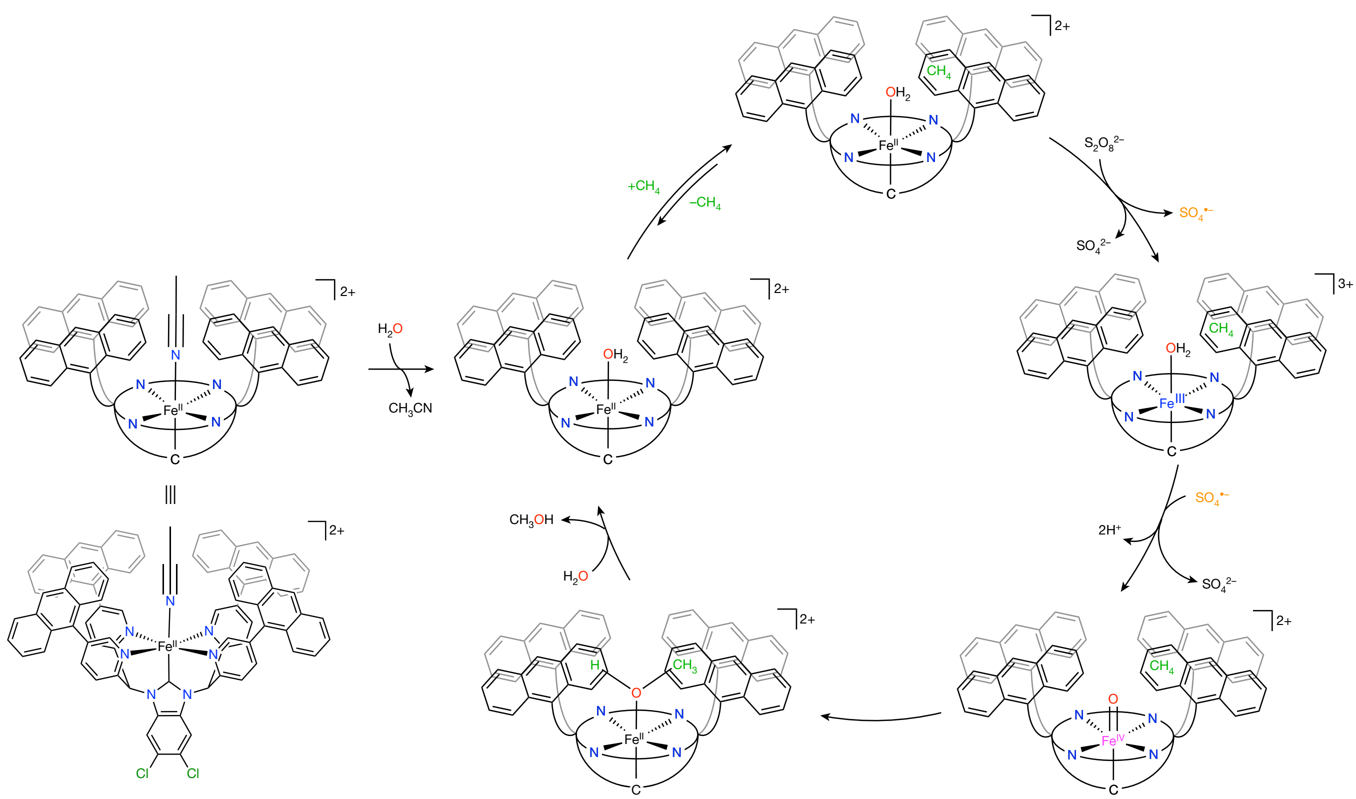

Fig. 3 | Proposed mechanism for the catch-and-release oxidation of CH_4 by 3-AN and $S_2O_8^{2-}$. In this mechanism, a hydrophobic CH_4 molecule is captured in the hydrophobic SCS of **3**-OH_2 formed by ligand substitution of CH_3CN in **3**-AN with H_2O. **3**-OH_2 undergoes PCET oxidation to generate the Fe^{IV}–oxo complex (**3**-O), which hydroxylates the CH_4 molecule trapped in the vicinity. The resultant methanol complex undergoes ligand substitution with H_2O to release the hydrophilic methanol molecule to the aqueous media to accomplish the catalytic cycle.

We assessed the thermodynamics of capturing CH_4 molecules in the hydrophobic SCSs of **3**-OD_2 by performing titration experiments at various temperatures using **3**-OD_2 in D_2O:CD_3CN (1:1, v/v; 600 μl) containing CH_4. We analysed the variations in the chemical shift of the CH_4 ^1H NMR signal after increasing the concentration of **3**-OD_2 to determine the association constant, K_a (Extended Data Fig. 3 and Supplementary Fig. 32), for each temperature[29] (equation (1) in Methods). On the basis of these data, we determined the thermodynamic parameters determined using van 't Hoff plots and these were found to be $\Delta H° = -24 \pm 1$ kJ mol^{-1} and $\Delta S° = -19 \pm 4$ J K^{-1} mol^{-1} (Extended Data Fig. 3e). These values are comparable with those reported for the encapsulation of CH_4 in a self-assembling superstructure ($\Delta H° = -38$ kJ mol^{-1} and $\Delta S° = -84$ J K^{-1} mol^{-1}) (ref. 30). The results described above provide evidence for the formation of adducts between **3**-OD_2 and gaseous alkanes in the aqueous medium. Furthermore, the corresponding association constants, K_a^{H} and K_a^{Mes}, for the entrapment of CH_4 by **1**-OD_2 and **2**-OD_2, were also determined to be less than 10 M^{-1} and $(1.7 \pm 0.4) \times 10^2$ M^{-1} at 298 K, respectively (Extended Data Fig. 3f,g).

We investigated the kinetics of the catalytic oxidation of CH_4 by **3**-OH_2 in H_2O:CH_3CN (95:5, v/v) at 323 K to gain further insights into the oxidation process. We found the rate constant (k_H^{Ant}) of CH_4 oxidation by **3**-OD_2 to be $(2.8 \pm 0.1) \times 10^{-6}$ s^{-1} (see Methods and Extended Data Fig. 1a–c). We also performed a kinetic isotope effect (KIE) analysis using CD_4 in the same aqueous medium (H_2O:CH_3CN (95:5, v/v)) at 323 K. The k_D^{Ant} value was determined to be $(7.6 \pm 0.8) \times 10^{-8}$ s^{-1} (see Methods and Extended Data Fig. 1d–f). The oxidation of CD_4 was slower than that of CH_4. The KIE value (k_H^{Ant}/k_D^{Ant}) for CH_4 oxidation by **3**-OH_2 was determined to be 37. This large KIE value indicates that the abstraction of a hydrogen atom from a C–H bond of CH_4 was a component of the rate-determining step for the overall process. It should also be noted that this extremely large KIE value indicates that non-classical hydrogen atom tunnelling is involved in the CH_4 oxidation reaction, as has previously been reported for intermediate Q, which is the reactive intermediate to oxidize CH_4 in the sMMO system[31].

The reactive species formed by the two-electron oxidation of **3**-OH_2 was characterized by cold-spray ionization time-of-flight mass spectrometry, microscopic Raman, UV–vis, electron spin resonance (ESR) and ^1H NMR spectroscopies; these analyses indicated the formation of a triplet Fe^{IV}–oxo complex, **3**-O (Methods, Extended Data Fig. 4 and Supplementary Figs. 33–35). Furthermore, the kinetic studies showed that **3**-O generated in situ immediately reacted with CH_4 (Supplementary Figs. 36 and 37). We also explained the properties of **3**-O by carrying out density functional theory (DFT) calculations for the Fe^{IV}–oxo complex derived from **3**-OH_2. We optimized the structure of triplet **3**-O derived from the proton-coupled electron-transfer (PCET) oxidation of **3**-OH_2 and performed DFT calculations to ascertain an energy minimum (Supplementary Fig. 38). In the optimized structure, the spin density of **3**-O was determined to be localized primarily at the Fe centre (1.14) and terminal oxo ligand (0.92) (Supplementary Table 2). The high spin density on the terminal oxo ligand and the small bond order (1.5) between the Fe centre and terminal O ligand suggest that **3**-O involves a larger contribution of an Fe^{III}(O·) electronic structure compared with typical Fe^{IV}(O) complexes, as reflected by the lower energy of Raman scattering (799 cm^{-1}) derived from the Fe–O bond[32,33]. This leads to improved CH_4 oxidation activity.

The energy profile for CH_4 oxidation by **3**-O as obtained from DFT calculations is shown in Extended Data Fig. 5. In this process, a CH_4 molecule trapped in the SCS undergoes hydrogen atom transfer to the Fe^{IV}(O) moiety to generate an Fe^{III}(OH) complex and a methyl radical (CH_3·) as an intermediate ('Int' in Extended Data Fig. 5). The hydrogen atom transfer reaction proceeds through a transition state ('TS' in Extended Data Fig. 5) in conjunction with a barrier calculated to be 19.2 kcal mol^{-1}. Finally, the hydroxo ligand bound to the Fe^{III} centre forms a C–O bond with a CH_3· radical to afford an Fe^{II}–CH_3OH complex as the product (Extended Data Fig. 5). Furthermore, barriers of transition states and intermediates for the CH_4 oxidation catalysed by **1**-OH_2 and **2**-OH_2 were calculated to be comparable with those by **3**-OH_2 (Supplementary Table 3). Thus, the reactivity of the Fe^{IV}=O moieties formed for the three catalysts should be comparable based on the same first coordination sphere, although **3**-O has the highest CH_4 oxidation reactivity. Furthermore, the Fe^{II}–CH_3OH complex derived from **3**-O was calculated to be more stable by approximately 7 kcal mol^{-1} than those derived from **1**-O and **2**-O (Supplementary Table 3). Therefore, the role of the hydrophobic SCS of **3**-O is very important for enhancing the reactivity by trapping a CH_4 molecule near the Fe centre.

On the basis of the results described above, we propose a mechanism for CH_4 oxidation using **3**-AN as a precatalyst in H_2O:CH_3CN (95:5, v/v), as shown in Fig. 3. In the first step, an AN ligand of **3**-AN is substituted by an aqua ligand in the aqueous medium. The Fe^{II}–aqua complex, **3**-OH_2, is also assumed to undergo PCET oxidation to afford the corresponding Fe^{IV}(O) species with an Fe^{III}(O·) character. A CH_4 molecule captured in the hydrophobic SCS is oxidized through C–H bond cleavage—this being the rate-determining step—to afford CH_3OH. In the final step, the weakly bound hydrophilic CH_3OH molecule is substituted by a H_2O molecule from the solvent and released to the aqueous medium to regenerate **3**-OH_2.

Our approach to efficient and selective catalytic two-electron oxidation of gaseous alkanes, on the basis of catalyst SCSs differentiating between hydrophobic substrates and hydrophilic products, demonstrates the viability of a catch-and-release mechanism when targeting natural gas. We anticipate that further development of this strategy might result in efficient and selective catalytic processes that can use naturally abundant carbon feedstocks.

Online content

Any methods, additional references, Nature Portfolio reporting summaries, source data, extended data, supplementary information, acknowledgements, peer review information; details of author contributions and competing interests; and statements of data and code availability are available at https://doi.org/10.1038/s41586-023-05821-2.

1. Schwach, P., Pan, X. & Bao, X. Direct conversion of methane to value-added chemicals over heterogeneous catalysts: challenges and prospects. *Chem. Rev.* **117**, 8497–8520 (2017).
2. Ravi, M., Ranocchiari, M. & van Bokhoven, J. A. The direct catalytic oxidation of methane to methanol—a critical assessment. *Angew. Chem. Int. Ed.* **56**, 16464–16483 (2017).
3. Riaz, A., Zahedi, G. & Klemeš, J. J. A review of cleaner production methods for the manufacture of methanol. *J. Clean. Prod.* **57**, 19–37 (2013).
4. Wang, B., Albarracín-Suazo, S., Pagán-Torres, Y. & Nikolla, E. Advances in methane conversion processes. *Catal. Today* **285**, 147–158 (2017).
5. Shilov, A. E. & Shul'pin, G. B. Activation of C–H bonds by metal complexes. *Chem. Rev.* **97**, 2879–2932 (1997).
6. Periana, R. A. et al. Platinum catalysts for the high-yield oxidation of methane to a methanol derivative. *Science* **280**, 560–564 (1998).
7. Mironov, O. A. et al. Using reduced catalysts for oxidation reactions: mechanistic studies of the "Periana-catalytica" system for CH_4 Oxidation. *J. Am. Chem. Soc.* **135**, 14644–14658 (2013).
8. Gunsalus, N. J. et al. Homogeneous functionalization of methane. *Chem. Rev.* **117**, 8521–8573 (2017).
9. Horn, R. & Schlögl, R. Methane activation by heterogeneous catalysis. *Catal. Lett.* **145**, 23–39 (2015).
10. Arakawa, H. et al. Catalysis research of relevance to carbon management: progress, challenges, and opportunities. *Chem. Rev.* **101**, 953–996 (2001).
11. Rosenzweig, A. C., Frederick, C. A., Lippard, S. J. & Nordlund, P. Crystal structure of a bacterial non-haem iron hydroxylase that catalyses the biological oxidation of methane. *Nature* **366**, 537–543 (1993).
12. Whittington, D. A., Rosenzweig, A. C., Frederick, C. A. & Lippard, S. J. Xenon and halogenated alkanes track putative substrate binding cavities in the soluble methane monooxygenase hydroxylase. *Biochemistry* **40**, 3476–3482 (2001).
13. Banerjee, R. & Lipscomb, J. D. Small-molecule tunnels in metalloenzymes viewed as extensions of the active site. *Acc. Chem. Res.* **54**, 2185–2195 (2021).
14. Zimmermann, T., Soorholtz, M., Bilke, M. & Schüth, F. Selective methane oxidation catalyzed by platinum salts in oleum at turnover frequencies of large-scale industrial processes. *J. Am. Chem. Soc.* **138**, 12395–12400 (2016).
15. Díaz-Urrutia, C. & Ott, T. Activation of methane: a selective industrial route to methanesulfonic acid. *Science* **363**, 1326–1329 (2019).

16. Luo, Y.-R. *Handbook of Bond Dissociation Energies in Organic Compounds* 1st edn (CRC, 2002).
17. Agarwal, N. et al. Aqueous Au-Pd colloids catalyze selective CH_4 oxidation to CH_3OH with O_2 under mild conditions. *Science* **358**, 223–227 (2017).
18. Jin, Z. et al. Hydrophobic zeolite modification for in situ peroxide formation in methane oxidation to methanol. *Science* **367**, 193–197 (2020).
19. Snyder, B. E. R. et al. The active site of low-temperature methane hydroxylation in iron-containing zeolite. *Nature* **536**, 317–321 (2016).
20. Shan, J. et al. Mild oxidation of methane to methanol or acetic acid on supported isolated rhodium catalysts. *Nature* **551**, 605–608 (2017).
21. Sushkevich, V. L., Palagin, D., Ranocchiari, M. & van Bokhoven, J. A. Selective anaerobic oxidation of methane enables direct synthesis of methanol. *Science* **356**, 523–527 (2017).
22. Chen, Y.-H., Wu, C.-Q., Sung, P.-H., Chan, S. I. & Chen, P. P.-Y. Turnover of a methane oxidation tricopper cluster catalyst: implications for the mechanism of the particulate methane monooxygenase (pMMO). *ChemCatChem* **12**, 3088–3096 (2020).
23. Sorokin, A. B., Kudrik, E. V. & Bouchu, D. Bio-inspired oxidation of methane in watercatalysed by *N*-bridged diiron phthalocyanine complex. *Chem. Commun.* **2008**, 2562–2564 (2008).
24. İşci, Ü. et al. Site-selective formation of an iron(IV)–oxo species at the more electron-rich iron atom of heteroleptic μ-nitride diiron phthalocyanines. *Chem. Sci.* **6**, 5063–5075 (2015).
25. Afanasiev, P. & Sorokin, A. B. μ-Nitrido diiron macrocyclic platform: particular structure for particular catalysis. *Acc. Chem. Res.* **49**, 583–593 (2016).
26. Friedle, S., Reisner, E. & Lippard, S. J. Current challenges of modelling diiron enzyme active sites for dioxygen activation by biomimetic synthetic complexes. *Chem. Soc. Rev.* **39**, 2768–2779 (2010).
27. Fujisaki, H. et al. Selective catalytic $2e^-$-oxidation of organic substrates by an Fe^{II} complex having an *N*-heterocyclic carbene ligand in water. *Chem. Commun.* **56**, 9783–9786 (2020).
28. Garal, L., Dutasta, J.-P. & Collet, A. Complexation of methane and chlorofluorocarbons by cryptophane-A in organic solution. *Angew. Chem. Int. Ed.* **32**, 1169–1171 (1993).
29. Kano, K., Kitae, T., Shimofuri, Y., Tanaka, N. & Mineta, Y. Complexation of polyvalent cyclodextrin ions with oppositely charged guests: entropically favourable complexation due to dehydration. *Chem. Eur. J.* **6**, 2705–2713 (2000).
30. Branda, N., Wyler, R. & Rebek, J. Jr Encapsulation of methane and other small molecules in a self-assembling superstructure. *Science* **263**, 1267–1268 (1994).
31. Brazeau, B. J., Wallar, B. J. & Lipscomb, J. D. Unmasking of deuterium kinetic isotope effects on the methane monooxygenase compound Q reaction by site-directed mutagenesis of component B. *J. Am. Chem. Soc.* **123**, 10421–10422 (2001).
32. Li, J.-L., Zhang, X. & Huang, X.-R. Mechanism of benzene hydroxylation by high-valent bare $Fe^{IV}=O^{2+}$: explicit electronic structure analysis. *Phys. Chem. Chem. Phys.* **14**, 246–256 (2012).
33. Shimoyama, Y. & Kojima, T. Metal–oxyl species and their possible roles in chemical oxidations. *Inorg. Chem.* **58**, 9517–9542 (2019).
34. Nash, T. The colorimetric estimation of formaldehyde by means of the Hantzsch reaction. *Biochem. J.* **55**, 416–421 (1953).

Methods

Synthesis of $[Fe^{II}(^{Mes}PY_4Cl_2BIm)(CH_3CN)](PF_6)_2$ (2-AN)

To a suspension of Fe^{II} acetate (161 mg, 1.0 mmol) in dimethyl sulfoxide (DMSO; 5 ml), $^{Mes}PY_4Cl_2BIm{\cdot}H{\cdot}Br$ (100 mg, 0.10 mmol; see Supplementary Information) was added. The mixture was stirred at room temperature for 24 h in the dark. After the addition of KPF_6 (854 mg, 4.6 mmol) and distilled water (20 ml), the reaction mixture was filtered through a membrane filter to obtain a red solid. The crude product was re-crystallized from CH_3CN/1,2-dimethoxyethane (DME) to obtain pale-red crystals of **2**-AN (70 mg, 0.050 mmol) with a 50% yield. ^1H NMR (CD_3CN): $\delta = 1.62$ (s, 12H, CH_3), 1.80 (s, 12H, CH_3), 2.24 (s, 12H, CH_3), 6.84 (s, 4H, *m*-H of Mes), 6.90 (s, 4H, *m*-H of Mes), 7.53 (dd, $J = 8, 2$ Hz, 4H, 3-H of Pyr), 7.71 (s, 2H, C*H*-Pyr), 7.93 (d, $J = 8$ Hz, 4H, 4-H of Pyr), 8.45 (s, 2H, 5,8-H of BnImd), 9.09 (d, $J = 2$ Hz, 4H, 6-H of Pyr). UV–vis (CH_3CN): λ_{max} (nm) = 342, 400, 454. ESI-TOF-MS (CH_3CN): $m/z = 545.67$ (sim for $[M - 2PF_6]^{2+}$: 545.69). Elemental analysis. Calculated for $C_{67}H_{63}Cl_2N_7Fe{\cdot}2PF_6{\cdot}H_2O$: H 4.68, C 57.44, N 7.00; found: H 4.45, C 57.49, N 7.23.

Synthesis of $[Fe^{II}(^{Mes}PY_4Cl_2BIm)(PhCN)](PF_6)_2$ (2-BN)

1,4-Dioxane was added slowly to a solution of **2**-AN (5.0 mg, 3.6 μmol) in PhCN (1 ml) to obtain a red powder of **2**-BN. The crude product was re-crystallized from CH_2Cl_2/hexane to obtain pale-red crystals of **2**-BN (2.0 mg, 2.0 μmol) with a 55% yield. ^1H NMR (CD_2Cl_2): $\delta = 1.56$ (s, 12H, CH_3), 1.78 (s, 12H, CH_3), 2.23 (s, 12H, CH_3), 6.78 (s, 4H, *m*-H of Mes), 6.83 (s, 4H, *m*-H of Mes), 7.47 (t, $J = 7$ Hz, 2H, *m*-H of PhCN), 7.61 (dd, $J = 8, 2$ Hz, 4H, 3-H of Pyr), 7.65 (m, 3H, *o*, *p*-H of PhCN), 8.06 (s, 2H, C*H*-Pyr), 8.30 (d, $J = 8$ Hz, 4H, 4-H of Pyr), 8.63 (s, 2H, 5,8-H of BnImd), 8.76 (d, $J = 2$ Hz, 4H, 6-H of Pyr). ESI-TOF-MS (acetone): $m/z = 576.60$ (sim for $[M - 2PF_6]^{2+}$: 576.69). Elemental analysis. Calculated for $C_{70}H_{57}Cl_2N_7Fe{\cdot}2PF_6{\cdot}0.5CH_2Cl_2{\cdot}0.5H_2O$: H 4.22, C 60.12, N 6.96; found: H 4.04, C 60.10, N 6.66.

Synthesis of $[Fe^{II}(^{Ant}PY_4Cl_2BIm)(CH_3CN)](PF_6)_2$ (3-AN)

To a suspension of Fe^{II} acetate (132.9 mg, 0.76 mmol) in DMSO (5 ml), $^{Ant}PY_4Cl_2BIm{\cdot}H{\cdot}Br$ (100 mg, 0.076 mmol; see Supplementary Information) was added and the mixture was stirred at 40 °C for 24 h in the dark. After the addition of KPF_6 (703 mg, 3.8 mmol) and distilled water (20 ml), the reaction mixture was passed through a membrane filter to obtain a red solid. The crude product was re-crystallized from CH_3CN/DME and pale-red crystals of **3**-AN (70 mg, 0.036 mmol) were obtained with a 48% yield. ^1H NMR (dmso-d_6): $\delta = 6.85$ (td, $J = 8, 4$ Hz, 4H, 7-H of Ant), 7.05 (d, $J = 9$ Hz, 4H, 8-H of Ant), 7.25–7.30 (m, 12H, 1,2,6-H of Ant), 7.41 (td, $J = 8, 4$ Hz, 4H, 3-H of Ant), 7.81 (dd, $J = 8, 2$ Hz, 4H, 4-H of Pyr), 7.91 (d, $J = 8$ Hz, 4H, 5-H of Ant), 7.96 (d, $J = 8$ Hz, 4H, 4-H of Ant), 8.06 (s, 2H, C*H*-Pyr), 8.22 (d, $J = 8$ Hz, 4H, 3-H of Pyr), 8.42 (s, 4H, 10-H of Ant), 8.69 (s, 2H, 5,8-H of BnImd), 9.27 (d, $J = 2$ Hz, 4H, 6-H of Pyr). UV–vis (CH_3CN): λ_{max} (nm) = 331, 386, 412. ESI-TOF-MS (CH_3CN): $m/z = 662.64$ (sim for $[M - 2PF_6]^{2+}$: $m/z = 662.64$). Elemental analysis. Calculated for $C_{87}H_{55}Cl_2N_7Fe{\cdot}2PF_6{\cdot}2H_2O$: H 3.66, C 63.25, N 6.07; found: H 3.49, C 63.46, N 6.03.

Synthesis of $[Fe^{II}(^{Ant}PY_4Cl_2BIm)(PhCN)](PF_6)_2$ (3-BN)

1,4-Dioxane was added slowly by vapour diffusion to a solution of **3**-AN (5.0 mg, 2.6 μmol) in PhCN (1 ml) to obtain red crystals of **3**-BN (1.5 mg, 1.3 μmol) with a 55% yield. ^1H NMR (CD_2Cl_2): $\delta = 6.70$ (td, $J = 8, 4$ Hz, 4H, 7-H of Ant), 6.88–6.94 (m, 12H, 1,2,6-H of Ant), 7.03 (d, $J = 9$ Hz, 4H, 8-H of Ant), 7.23 (td, $J = 8, 4$ Hz, 4H, 3-H of Ant), 7.47 (t, $J = 7$ Hz, 2H, *m*-H of PhCN), 7.59 (dd, $J = 8, 2$ Hz, 4H, 4-H of Pyr), 7.65 (m, 3H, *o*,*p*-H of PhCN), 7.84 (s, 2H, C*H*-Pyr), 7.87 (d, $J = 8$ Hz, 4H, 5-H of Ant), 7.93 (d, $J = 8$ Hz, 4H, 4-H of Ant), 8.32 (s, 4H, 10-H of Ant), 8.54 (d, $J = 8$ Hz, 4H, 3-H of Pyr), 8.81 (s, 2H, 5,8-H of BnImd), 8.90 (d, $J = 2$ Hz, 4H, 6-H of Pyr). ESI-TOF-MS (acetone): $m/z = 692.57$ (sim for $[M - 2PF_6]^{2+}$: $m/z = 692.64$). Anal. Calcd. for $C_{92}H_{57}Cl_2N_7Fe{\cdot}PhCN{\cdot}2PF_6{\cdot}6H_2O$: H 3.97, C 61.82, N 6.14; found: H 4.22, C 61.87, N 6.35.

Incubation of the catalysts in an aqueous medium

When **1**-AN, **2**-AN and **3**-AN were incubated for 5 min in $H_2O:CH_3CN$ (95:5, v/v) at 323 K, absorption spectra of the complexes changed as shown in Supplementary Fig. 8. The ESI-TOF-MS spectra also changed: the peak clusters assigned to the corresponding AN complexes disappeared (Supplementary Figs. 9–11). Furthermore, the ^1H-NMR spectra of **1**-AN after incubation for 5 min in D_2O:acetone-d_6 (95:5, v/v) at 323 K showed a singlet due to the dissociated CH_3CN, indicating the formation of the corresponding D_2O-bound Fe^{II}–aqua ($Fe^{II}–OD_2$) complex, **1**-OD_2 (Supplementary Fig. 12). In the square-wave voltammograms of the Fe^{II} complexes in $H_2O:CH_3CN$ (95:5, v/v) at 323 K, the oxidation waves assigned to the corresponding Fe^{III} or Fe^{II} couple were observed at +0.75 V (compared with SCE) for **1**-OH_2, +0.86 V for **2**-OH_2 and +0.82 V for **3**-OH_2, reflecting the similarity of the electronic environments of the iron centres in the complexes as mentioned above (Supplementary Fig. 13).

General procedure for catalytic oxidation of gaseous alkanes

A schematic of the reaction set-up is shown in Supplementary Fig. 39. A 10-ml high-pressure-tolerable glass-tube reactor was charged with a solution of one of the catalysts (1.0 μM) and $Na_2S_2O_8$ (5.0 mM) as an oxidant in $D_2O:CD_3CN$ (95:5, v/v, 1.0 ml, pD was not adjusted). After passing one of the gaseous alkanes through the solution to force out air and saturate the solution with the gaseous alkane, the headspace of the reactor was filled with a gaseous alkane at the appropriate pressure. The reactions were performed at 323 K in a water bath. Qualitative and quantitative analyses of the reaction products were made by ^1H NMR spectroscopy using sodium 3-(trimethylsilyl)propanesulfonate (DSS) as an internal standard. The conversion of CH_4 was calculated based on the amount of CH_4 by the ideal gas law in the solution of $D_2O:CD_3CN$ (95:5, v/v, 2.9 ml) to be 4.1% as follows:

$$\text{Conversion of } CH_4\ (\%) = ([\text{Products}] \times 2.9\ \text{ml})/n \times 100$$
$$= 1.5 \times 10^{-3}/0.037 \times 100 = 4.1\%$$

where $n = 0.037$ mmol: the mole of CH_4 based on the ideal gas law ($P = 0.98$ MPa, $V = 0.1$ ml (gas phase), $R = 8.31 \times 10^3$ Pa l (K mol)$^{-1}$, $T = 323$ K), [Products] (0.51 mM) × 2.9 ml (liquid phase) = 1.5×10^{-3} mmol. Conditions: A 3-ml high-pressure-tolerable J. Young valve NMR tube was charged with a solution of one of the catalysts (0.05 mM) and $Na_2S_2O_8$ (250 mM) as an oxidant in $D_2O:CD_3CN$ for 6 h (95:5, v/v, 2.9 ml, pD was not adjusted). The selectivity of CH_3OH production under the same conditions was determined to be 83%.

Nuclear Overhauser effect experiments for investigation of interaction between 3-OD_2 and CH_4

To explain the capture of CH_4 molecules in the hydrophobic SCS of **3**-OD_2, we observed nuclear Overhauser effects (NOEs) in the ^1H NMR measurements using **3**-OD_2 (0.10 mM) and CH_4 (0.05 mM) in $D_2O:CD_3CN$ (1:1, v/v) at room temperature. Differential NOE spectra were obtained by saturating resonances giving the ^1H NMR signals of 5-H of the benzimidazole moiety at 8.69 ppm, methylene-H at 8.06 ppm, and 3-H and 4-H of the pyridine moieties at 8.22 and 7.81 ppm, respectively. The differential spectra between those with and without the irradiation show no correlation signals (Supplementary Figs. 20–23) and thus showed that these protons are not close to the CH_4 molecule. Another set of the differential NOE spectra was obtained by saturating resonances giving the ^1H NMR signals of aromatic protons of the anthracenyl groups at 8.42, 7.94, 7.41, 7.27, 7.05 and 6.85 ppm and that of 6-H of the pyridine moiety at 9.27 ppm. The differential spectra between those with and without the irradiation clearly indicate correlation signals (Supplementary Figs. 24–30). Thus, these protons should be close to the CH_4 molecule. These results indicate that a CH_4 molecule is captured inside the hydrophobic SCS constructed by the anthracenyl groups of **3**-OD_2 (Supplementary Fig. 31).

The K_a value for CH_4 capture

The K_a value for CH_4 capture by **3**-OD_2 at 298 K was determined to be $(2.1 \pm 0.4) \times 10^3$ M^{-1} (Extended Data Fig. 3a), which is relatively high compared with the values reported so far for CH_4 encapsulation[30,35]. The K_a values at 278 K, 308:K and 323 K were calculated to be $(4.0 \pm 0.5) \times 10^3$ M^{-1}, $(1.4 \pm 0.2) \times 10^3$ M^{-1} and $(0.9 \pm 0.1) \times 10^3$ M^{-1}, respectively (Extended Data Fig. 3b–d). The fitting curves in Extended Data Fig. 3a–d,f,g were calculated using equation (1).

$$\Delta\delta = \frac{\Delta\delta_\infty}{2K_a^R[CH_4]_0}\{1 + K_a^R[Fe^{II}] + K_a^R[CH_4]_0\{(1 + K_a^R[Fe^{II}] + K_a^R[CH_4]_0)^2 - 4K_a^{R^2}[Fe^{II}][CH_4]_0\}^{1/2}\} \quad (1)$$

Kinetic analysis of the catalytic oxidation of CH_4 and CD_4

Concentrations of the oxidation products were determined by gas chromatography–mass spectrometry (GC–MS) on the basis of a calibration curve using benzonitrile as an internal standard. Concentrations of CH_4 and CD_4 were calculated on the basis of the values reported[36] for the aqueous solution (0.25 MPa, 2.5 mM; 0.50 MPa, 5.0 mM; 0.75 MPa, 7.5 mM; 0.98 MPa, 9.8 mM). The product concentrations were plotted against the reaction time to obtain time profiles of the product formation. Least-squares linear fitting was conducted for the plots in the range of about 0 h to 3 h. The slopes of the fitting lines obtained were used to determine the initial reaction rates, v_0, of the CH_4 and CD_4 oxidation (Extended Data Fig. 1c,f). The initial rates, v_0, of the CH_4 and CD_4 oxidation by **3**-OD_2 at various CH_4 and CD_4 concentrations were determined by the time courses of the product concentration obtained by GC–MS and were plotted against the initial CH_4 or CD_4 concentrations to estimate the rate constants, k_H^{Ant} and k_D^{Ant} (Extended Data Fig. 1c,f). GC–MS: column, DB-Wax UI capillary column (30 m); career gas, helium; interface and detector temperature, 200 °C; temperature programme, 30 °C for 4 min, increasing to 200 °C at a rate of 50 °C min^{-1}, followed by 200 °C for 3.4 min.

One-electron-oxidized species of 3-OH_2

We measured an electron spin resonance (ESR) spectrum of a sample obtained by quick freezing a portion of a solution of catalytic CH_4 oxidation using **3**-OH_2 at 323 K in the presence of $Na_2S_2O_8$ in a H_2O:MeCN (95:5) mixed solvent. We detected an ESR signal at g = 2.492, 2.343 and 1.860 (Extended Data Fig. 4e). To assign the ESR signal, we separately prepared $[Fe^{III}(^{Ant}PY_4Cl_2BIm)(OH_2)]^{2+}$ from **3**-OH_2 by adding 1.2 equivalent (equiv.) of cerium(IV) ammonium nitrate (CAN) as the oxidant in MeCN:H_2O (3:1) at 298 K. The complex showed absorption bands at 700 nm (Extended Data Fig. 4d, blue line). On the basis of the increase in absorbance at 700 nm, the second-order rate constant for the formation of $[Fe^{III}(^{Ant}PY_4Cl_2BIm)(OH_2)]^{2+}$, k_2^{ET1}, was determined to be $(1.1 \pm 0.1) \times 10^7$ M^{-1} s^{-1} in a MeCN:H_2O (3:1) solution at 278 K (Supplementary Fig. 35a,b). The ESR signal of the Fe^{III}–OH_2 species (S = 1/2) was observed at g = 2.492, 2.343 and 1.860 (Extended Data Fig. 4e, blue line), consistent with those observed for the reaction mixture of the catalysis. All electron spin resonance (ESR spectra) were measured at 100 K. Microwave frequency, 9.572 GHz; microwave power, 1.0 mW; modulation frequency, 100.00 kHz; modulation amplitude, 3.00 G.

Characterization of 3-O

3-OH_2 was oxidized by CAN as an oxidant, which was used instead of $Na_2S_2O_8$ for the catalytic reactions, in a mixed solvent of CH_3CN:H_2O (3:1) at 278 K. In the cold-spray ionization time-of-flight mass spectrometry (CSI-TOF-MS) spectrum of **3**-O formed with CAN measured at 278 K, a peak cluster was observed at m/z = 648.96, assigned to $[\mathbf{3}\text{-O} - 2PF_6]^{2+}$ (sim: m/z = 649.14) (Extended Data Fig. 4a, top), as in the case of $Na_2S_2O_8$. When the formation of **3**-O was conducted with 5 equiv. of CAN in a mixed solvent of CH_3CN:$H_2{}^{18}O$ (3:1), the peak cluster in the CSI-TOF-MS spectrum shifted to m/z = 650.01, assignable to $[\mathbf{3}\text{-}^{18}\text{O} - 2PF_6]^{2+}$ (sim: m/z = 650.14) (Extended Data Fig. 4b).

When **3**-OH_2 was reacted with 1.2 equiv. of CAN in a MeCN:H_2O (3:1) solution at 278 K, a new absorption band appeared at 700 nm in the UV–vis spectrum, derived from the formation of the corresponding Fe^{III} complex, $[Fe^{III}(^{Ant}PY_4Cl_2BIm)(OH_2)]^{2+}$ (Extended Data Fig. 4d, blue line). Simultaneously, the absorption band of **3**-OH_2 at 420 nm disappeared. Furthermore, when **3**-OH_2 was treated with 5 equiv. of CAN in a MeCN:H_2O (3:1) mixed solvent at 278 K, a new absorption band was observed at 800 nm, derived from the formation[37] of **3**-O (Extended Data Fig. 4d, green line). On the basis of the increase in the absorbance at 800 nm, the first-order rate constant for the formation of **3**-O, k_1^{ET2}, was determined to be $(2.25 \pm 0.05) \times 10^{-1}$ s^{-1} in a MeCN:H_2O (3:1) solution at 278 K (Supplementary Fig. 35c,d).

The Raman spectrum of **3**-O in a CH_3CN:H_2O (3:1) solution at 298 K upon excitation at 532 nm exhibited a Raman scattering at 799 cm^{-1}, derived from the Fe–O bond stretching; the use of $H_2{}^{18}O$ caused a low-energy shift of the signal to 759 cm^{-1} (Extended Data Fig. 4c). The isotope shift ($\Delta\nu$) was calculated to be 40 cm^{-1}, which was consistent with the theoretical value ($\Delta\nu$ = 36 cm^{-1}). The Raman shift of the stretching band for the Fe–O bond of **3**-O was moderately smaller than those for other Fe^{IV}=O complexes reported so far (ν = 820–853 cm^{-1})[38,39], suggesting that **3**-O should have a weaker Fe–O bond than typical Fe^{IV}=O bonds. The excitation wavelength for the Raman measurements was 532 nm.

Because **3**-O was ESR silent under the conditions examined, we used the Evans method[40] based on ^{1}H NMR spectroscopy to estimate the magnetic susceptibility of **3**-O (Supplementary Fig. 34), which was formed by the treatment of **3**-OH_2 with 3 equiv. of CAN in D_2O:CD_3CN (1:3) at 278 K. The effective magnetic moment (μ_{eff}) of **3**-O was calculated to be 2.75μ_B, allowing us to confirm the spin state of **3**-O to be S = 1 (μ_{eff} calculated for the spin-only: 2.83μ_B).

Decomposition of 3-O

We also investigated the decomposition of **3**-O under catalytic conditions—in H_2O:CH_3CN (95:5, v/v) before and after addition of $Na_2S_2O_8$ at 323 K, in the absence of substrates. The ESI-TOF-MS spectrum of the reaction mixture was found to have a peak cluster at m/z = 649.02 (Supplementary Fig. 33b, filled red circle), which was assigned to **3**-O (sim for $[\mathbf{3}\text{-O} - 2PF_6]^{2+}$: m/z = 649.14). **3**-O underwent oxidative decomposition accompanied by the loss of the dipyridylmethyl arm of the NHC ligand as confirmed by the ESI-TOF-MS and ^{1}H NMR measurements of the reaction mixture after incubation for 3 h (Supplementary Fig. 33). The decomposition of **3**-O was also observed by a decrease in the absorbance at 800 nm accompanied by an increase in the absorbance at 700 nm, derived from the corresponding Fe^{III}–OH_2 species (Supplementary Fig. 36). On the basis of the decrease in absorbance at 800 nm, the first-order rate constant for the decomposition of **3**-O, k_{decomp}, was determined to be $(2.52 \pm 0.03) \times 10^{-4}$ s^{-1} in a MeCN:H_2O (3:1) solution at 278 K in the absence of substrates such as CH_4 (Supplementary Fig. 36). The decomposition was also monitored by ESI-TOF-MS and ^{1}H NMR measurements, which suggest the formation of a Fe^{II} species that has lost one dipyridylmethyl moiety (Supplementary Fig. 33).

Kinetic studies on the reaction of 3-O with CH_4

When injecting CH_4 after the formation of **3**-O by reaction with CAN, the broad absorption band at 800 nm decayed and a new band at 682 nm appeared that showed an isosbestic point at 753 nm as the reaction progressed between **3**-O and CH_4 (Supplementary Fig. 37a). The pseudo-first-order rate constant, k_1, for the reaction of **3**-O with an excess amount of CH_4 was determined to be $(1.24 \pm 0.02) \times 10^{-3}$ s^{-1}, on the basis of decrease of absorbance at 800 nm (Supplementary Fig. 37b). Therefore, **3**-O can react with CH_4 predominantly, because k_1 was five times larger than k_{decomp} of **3**-O.

Computational details

We performed the DFT calculations with the Gaussian 16 program package (revision C01)[41]. All geometry optimizations were carried out with the B3LYP functional[42,43]. We used the Wachters–Hay basis set[44,45] for Fe and the D95** basis set[46] for the other atoms. After geometry optimizations, we performed vibrational analyses for all reaction species to confirm stable and transition structures. Energy profiles of calculated pathways are presented as the Gibbs free energy (T = 323 K) considering the solvent effect of water on the basis of the polarizable continuum model[47] and the Grimme-D3 dispersion energy corrections[48]. We calculated the kinetic isotope effect (KIE) (k_H/k_D) for the H-atom abstraction from CH_4 or CD_4 using transition-state theory[49] as shown in equation (2).

$$\frac{k_{\mathrm{H}}}{k_{\mathrm{D}}}=\frac{(I^{R}_{x\mathrm{D}}I^{R}_{y\mathrm{D}}I^{R}_{z\mathrm{D}})^{1/2}}{(I^{R}_{x\mathrm{H}}I^{R}_{y\mathrm{H}}I^{R}_{z\mathrm{H}})^{1/2}}\frac{(I^{\#}_{x\mathrm{H}}I^{\#}_{y\mathrm{H}}I^{\#}_{z\mathrm{H}})^{1/2}}{(I^{\#}_{x\mathrm{D}}I^{\#}_{y\mathrm{D}}I^{\#}_{z\mathrm{D}})^{1/2}}\frac{q^{\mathrm{R}}_{\mathrm{D}}q^{\#}_{\mathrm{H}}}{q^{\mathrm{R}}_{\mathrm{H}}q^{\#}_{\mathrm{D}}}\exp\left(\frac{E^{\#}_{\mathrm{H}}-E^{\#}_{\mathrm{D}}}{RT}\right) \quad (2)$$

Here I, q and E indicate the moment of inertia, the vibrational partition function and the activation energy with thermal correction, respectively; R specifies the reactant complex; # indicates the transition state; the letters x, y and z correspond to the components of the three-dimensional space of each variable; H means the species including CH_4; D means the species including CD_4. The last exponential term is dominant in this equation because the other terms can be almost all cancelled between denominators and numerators.

The DFT-calculated KIE value at 323 K was 15 for CH_4 oxidation accompanied by hydrogen atom tunnelling, which is consistent with the experimental KIE value of 37 and so provides support for a tunnelling effect in the hydrogen atom transfer process.

Data availability

X-ray data are available free of charge from the Cambridge Crystallographic Data Centre under reference numbers CCDC-2106612 and 2106613. All other experimental, spectroscopic, crystallographic and computational data are available from the corresponding author upon request. Source data are provided with this paper.

35. Ruan, Y., Peterson, P. W., Hadad, C. M. & Badjić, J. D. On the encapsulation of hydrocarbon components of natural gas within molecular baskets in water. The role of C–H···π interactions and the host's conformational dynamics in the process of encapsulation. *Chem. Commun.* **50**, 9086–9089 (2014).
36. Duan, Z. & Mao, S. A thermodynamic model for calculating methane solubility, density and gas phase composition of methane-bearing aqueous fluids from 273 to 523 K and from 1 to 2000 bar. *Geochim. Cosmochim. Acta* **70**, 3369–3386 (2006).
37. Rohde, J.-U. et al. Crystallographic and spectroscopic characterization of a nonheme Fe(IV)–O complex. *Science* **299**, 1037–1039 (2003).
38. Sastri, C. V. et al. Axial ligand substituted nonheme Fe^{IV}=O complexes: observation of near-UV LMCT bands and Fe=O Raman vibrations. *J. Am. Chem. Soc.* **127**, 12494–12495 (2005).
39. Andris, E. et al. Trapping iron(III)–oxo species at the boundary of the "oxo wall": insights into the nature of the Fe(III)–O bond. *J. Am. Chem. Soc.* **140**, 14391–14400 (2018).
40. Evans, D. F. & Jakubovic, D. Water-soluble hexadentate Schiff-base ligands assequestrating agents for iron(III) and gallium(III). *J. Chem. Soc. Dalton Trans.* **1988**, 2927–2933 (1988).
41. Frisch, M. J. et al. *Gaussian 16* revision C.01 (Gaussian, 2009).
42. Becke, A. D. Density-functional thermochemistry. III. The role of exact exchange. *J. Chem. Phys.* **98**, 5648–5652 (1993).
43. Lee, C., Yang, W. & Parr, R. G. Development of the Colle–Salvetti correlation–energy formula into a functional of the electron density. *Phys. Rev. B* **37**, 785–789 (1988).
44. Wachters, A. J. H. Gaussian basis set for molecular wavefunctions containing third-row atoms. *J. Chem. Phys.* **52**, 1033–1036 (1970).
45. Hay, P. J. Gaussian basis sets for molecular calculations. The representation of 3*d* orbitals in transition-metal atoms. *J. Chem. Phys.* **66**, 4377–4384 (1977).
46. Dunning, T. H. Jr & Hay, P. J. in *Modern Theoretical Chemistry* Vol. 3 (ed. Schaefer, H. F. III), (Plenum, 1977).
47. Cossi, M., Barone, V., Cammi, R. & Tomasi, J. Ab initio study of solvated molecules: a new implementation of the polarizable continuum model. *Chem. Phys. Lett.* **255**, 327–335 (1996).
48. Grimme, S., Antony, J., Ehrlich, S. & Krieg, H. A consistent and accurate ab initio parameterization of density functional dispersion correction (DFT-D) for the 94 elements H-Pu. *J. Chem. Phys.* **132**, 154104 (2010).
49. Frost, A. A. & Pearson, R. G. *Kinetics and Mechanism* (Wiley, 1961).

Acknowledgements This work was supported by JST CREST (grant nos. JPMJCR16P1 and JPMJCR15P5) and by Grants-in-Aid (grant nos. 17H03027, 18K19089 and 21H01947) from the Japan Society for the Promotion of Science (JSPS). K.Y. and Y.S. acknowledge the MEXT projects of Cooperative Research Program of Network Joint Research Centre for Materials and Devices, Integrated Research Consortium on Chemical Sciences and the Elements Strategy Initiative to Form Core Research Centre. H.F. also acknowledges funding from JST SPRING (grant no. JPMJSP2124) and Research Fellowship for Young Scientists provided by JSPS (grant no. 22J10804). We thank Edanz (https://jp.edanz.com/ac) for editing a draft of this manuscript.

Author contributions T.K. conceived and directed the project. H.F. performed the experimental work and analysed the data. T.I. performed X-ray crystallographic analyses of the complexes. K.Y. and Y.S. performed the computational studies. H.K. contributed to kinetic studies. All of the authors discussed the results and H.F., T.I., Y.S. and T.K. prepared the manuscript.

Competing interests The authors declare no competing interests.

Additional information
Supplementary information The online version contains supplementary material available at https://doi.org/10.1038/s41586-023-05821-2.
Correspondence and requests for materials should be addressed to Takahiko Kojima.
Peer review information *Nature* thanks Christian Limberg and Marco Ranocchiari for their contribution to the peer review of this work. Peer reviewer reports are available.

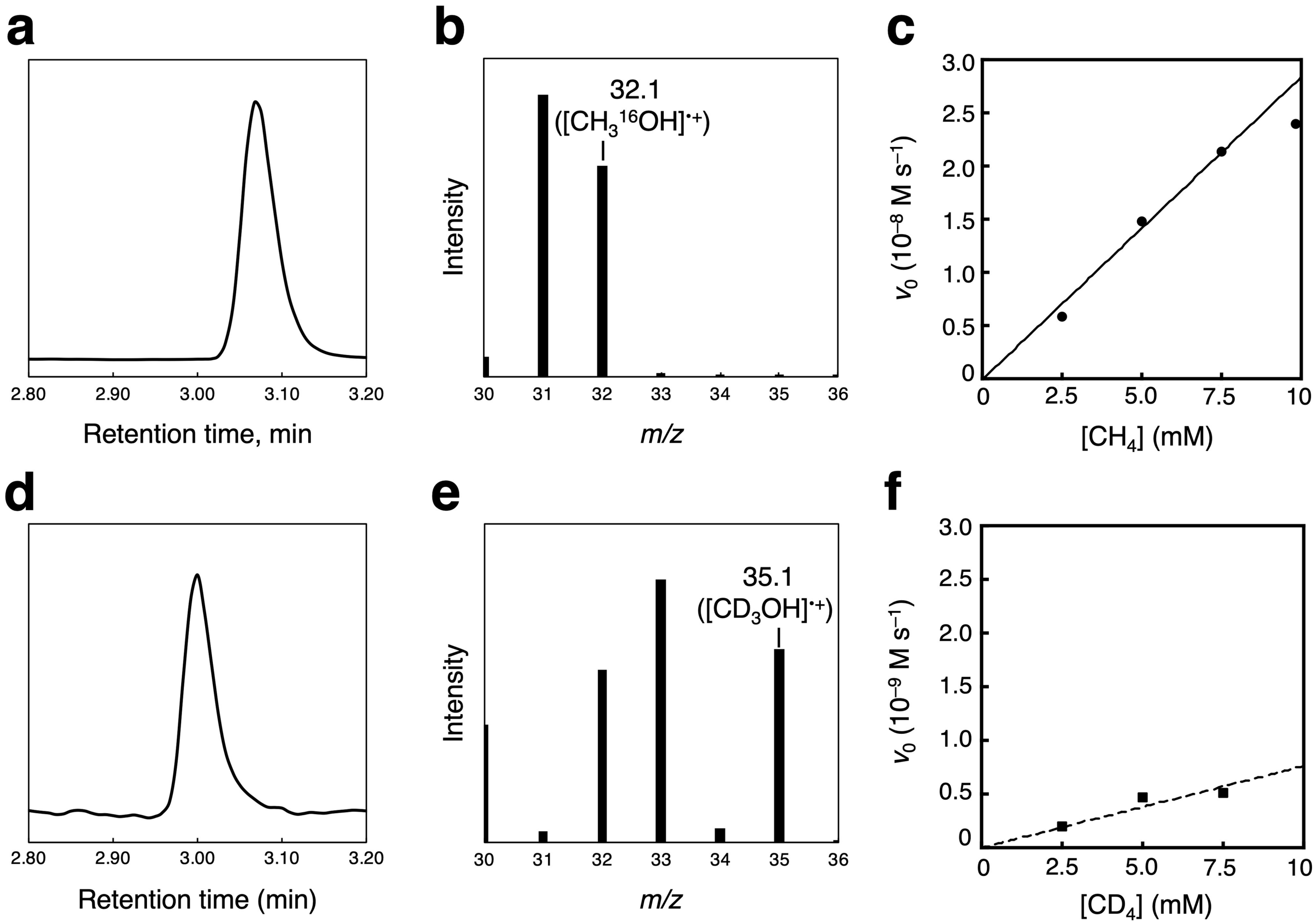

Extended Data Fig. 1 | Kinetic studies for the CH_4 oxidation. **a**, A GC-MS total-ion chromatogram for the reaction mixture of the CH_4 (0.75 MPa) oxidation by **3**-OH_2, obtained by gas chromatography equipped with electron-ionization (EI) mass detector (GC-MS). **b**, EI-MS spectrum of the fraction eluted at the retention time of 3.09 min in **a**. **c**, Dependence of the initial rates, υ_0, for the catalytic oxidation of CH_4 using **3**-OH_2, on the initial CH_4 concentration, [CH_4]. [CH_4] were calculated on the basis of the values reported for aqueous solutions (0.25 MPa: 2.5 mM, 0.50 MPa: 5.0 mM, 0.75 MPa: 7.5 mM, and 0.98 MPa: 9.8 mM)[36]. The slope of the line, in which the υ_0 value at 0.98 MPa (9.8 mM) was omitted, since the initial rate showed saturation behaviour against the [CH_4], is calculated to obtain the rate constant, $k^{Ant}{}_{H}$, as $(2.8 \pm 0.1) \times 10^{-6}$ s^{-1}. **d**, A GC-MS total-ion chromatogram for the reaction mixture of CD_4 (0.75 MPa) oxidation by **3**-OH_2. **e**, EI-MS spectrum of the fraction eluted at the retention time of 3.00 min in **d**. **f**, Dependence of the initial rates, υ_0, for the catalytic oxidation of CD_4 using **3**-OH_2, on the initial CD_4 concentration, [CD_4]. The slope of the line is calculated to obtain the rate constant, $k^{Ant}{}_{D}$, as $(7.6 \pm 0.8) \times 10^{-8}$ s^{-1}. Reaction conditions: [**3**-OH_2] = 0.010 mM, [$Na_2S_2O_8$] = 50 mM, solvent = H_2O/CH_3CN (95:5, v/v; pD was not adjusted), T = 323 K, reaction time: 3 h.

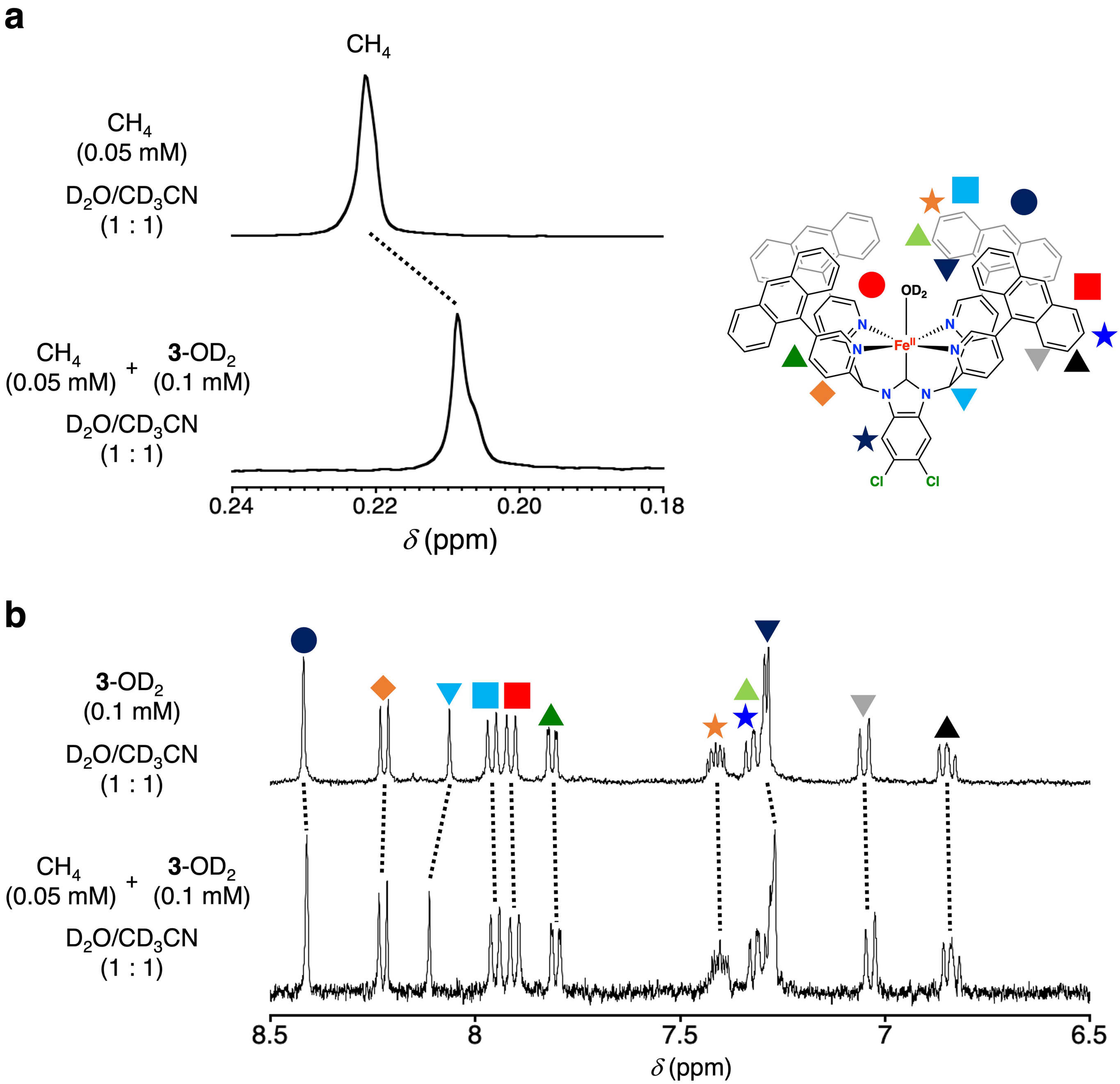

Extended Data Fig. 2 | Entrapment of CH_4 with 3-OD_2 monitored by ^{1}H NMR spectroscopy. a, ^{1}H NMR spectra of CH_4, whose concentration was estimated to be 0.05 mM, in D_2O/CD_3CN (1:1, v/v) in the absence (top) and presence (bottom) of **3**-OD_2 (0.1 mM) at 298 K. **b**, ^{1}H NMR spectra in D_2O/CD_3CN (1:1, v/v) of **3**-OD_2 (0.1 mM) at 298 K before (top) and after (bottom) bubbling CH_4, whose concentration was estimated to be 0.05 mM.

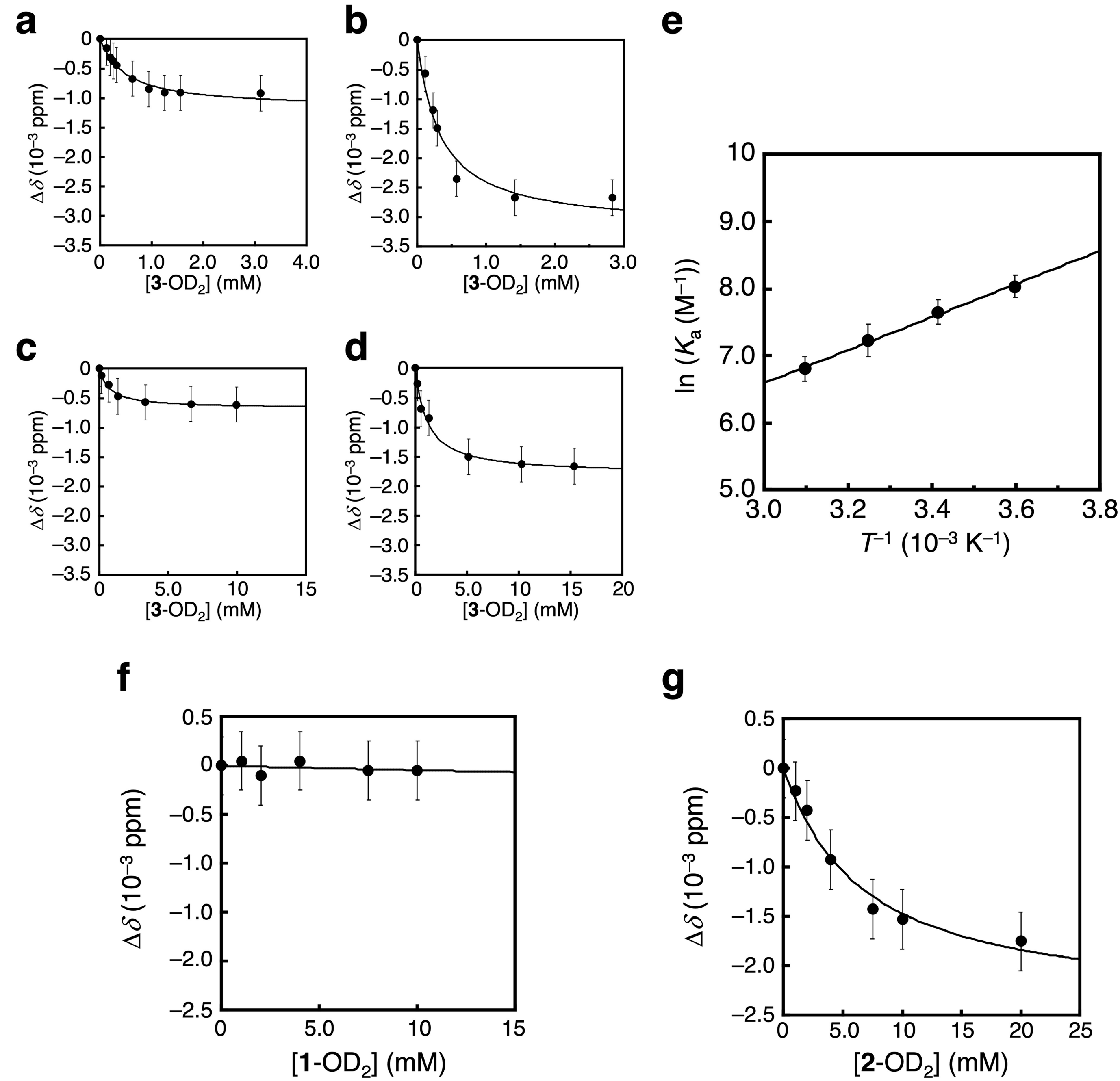

Extended Data Fig. 3 | Analysis of the chemical shift change for the ^{1}H NMR signal of CH_4 upon addition of the Fe^{II}-NHC complexes. Plots of the chemical shift change for the ^{1}H NMR signal of CH_4 against the concentration of **3**-OD_2 at 298 K (**a**), 278 K (**b**), 308 K (**c**), and 323 K (**d**) in D_2O/CD_3CN (1:1, v/v). **e**, van't Hoff plot for the association of CH_4 with **3**-OD_2. Plots of the chemical shift change for the ^{1}H NMR signal of CH_4 against the concentration of **1**-OD_2 (**f**) and **2**-OD_2 (**g**) at 298 K. The fitting curves (solid lines) in **a** – **d**, **f** & **g** are calculated using equation (1) in the Methods as described previously[29]. The error bars in the plots represent the digital resolution for the ^{1}H NMR spectroscopy under the conditions.

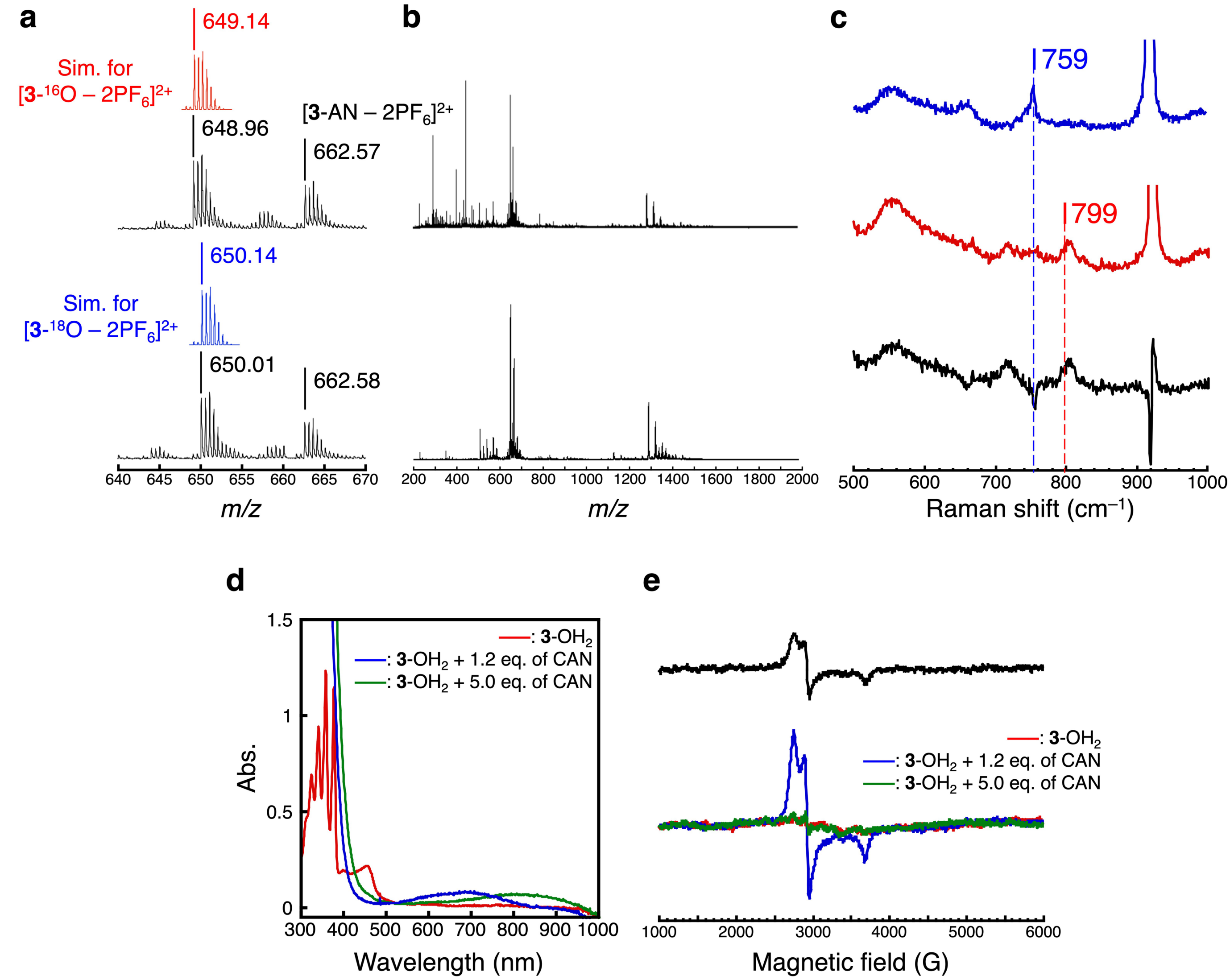

Extended Data Fig. 4 | Spectroscopic data for 3-O. CSI-TOF-MS spectra of **3**-^{16}O (top) and **3**-^{18}O (bottom), obtained from oxidation of **3**-OH_2 with 5 equiv of CAN in a mixed solvent of CH_3CN:$H_2{}^{16}O$ (3:1) and CH_3CN:$H_2{}^{18}O$ (3:1), diluted with CH_3CN and measured at 278 K and their simulations (**a**) and the full-range spectra (*m*/*z* = 200 – 2000) (**b**). **c**, Microscopic Raman spectra of **3**-O, formed from **3**-OH_2 with 5 equiv of CAN in CH_3CN:$H_2{}^{16}O$ (3:1, v/v) (red) or CH_3CN:$H_2{}^{18}O$ (3:1, v/v) (blue), at 298 K and the differential spectrum (black). **d**, UV-vis spectra of **3**-OH_2 (red); $[Fe^{III}(^{Ant}PY_4Cl_2BIm)(OH_2)]^{2+}$ (blue), generated in-situ from **3**-OH_2 by addition of 1.2 equiv of CAN; **3**-O (green), generated in-situ from **3**-OH_2 by addition of 5 equiv of CAN, in CH_3CN:H_2O (3:1). **e**, (top) ESR spectrum of the reaction mixture, quickly frozen during the catalytic oxidation of CH_4 (3.5 mM) by **3**-OH_2 (0.1 mM) in the presence of $Na_2S_2O_8$ (50 mM) in H_2O:CH_3CN (95:5) at 323 K; (bottom) ESR spectra of **3**-OH_2 (red), $[Fe^{III}(^{Ant}PY_4Cl_2\text{-}BIm)(OH_2)]^{2+}$ (blue) and **3**-O (green), obtained from oxidation of **3**-OH_2 with 1.2 equiv and 5 equiv of CAN, respectively, in CH_3CN:H_2O (3:1) (bottom).

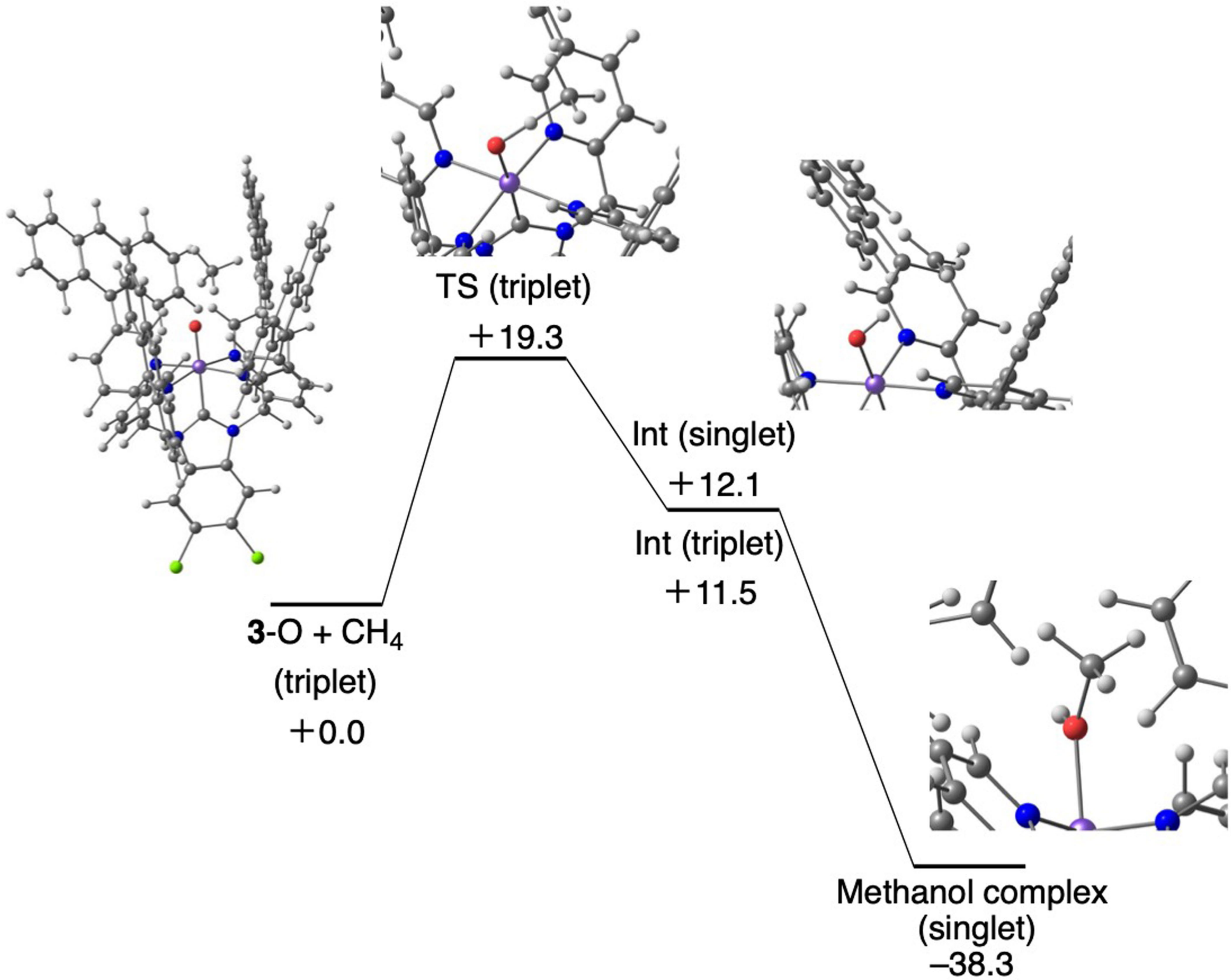

Extended Data Fig. 5 | DFT-calculated energy profile for the rate-determining HAT step in the CH_4 oxygenation process. Relative free energy values are given in kcal mol^{-1} with respect to a reactant complex consisting of the Fe^{IV}-oxo complex (**3**-O) and one trapped methane molecule. Here, "TS" and "Int" refer to a transition state generated during methane oxygenation and an intermediate consisting of the Fe^{III}-OH complex and the methyl radical, respectively.

Article

Extended Data Table 1 | Summary of the product concentrations obtained from the oxidation reactions of gaseous alkanes in the absence and presence of iron salts or 3-OD$_2$ in a mixed solvent of D$_2$O/CD$_3$CN (95/5)

Substrate	$BDE_{C\text{-}H}$[*,†]	Products	Catalyst			
			None	$Fe(NO_3)_3 \cdot 9H_2O$	$Fe(ClO_4)_2 \cdot 6H_2O$	**3**-OD_2
			[Product] (mM)			
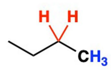 *n*-Butane (3.9 mM)	98.3 100.7	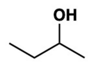	0.01	0.05	0.02	1.5
		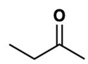	0.02	0.04	0.08	0.51
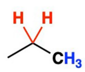 Propane (4.2 mM)	98.1 99.9	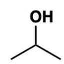	N.D.	0.03	0.05	1.1
		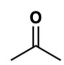	0.03	0.04	0.12	0.20
C_2H_6 Ethane (4.7 mM)	100.5	C_2H_5OH	N.D.	0.02	0.05	0.87
		CH_3COOH	0.02	0.01	0.10	0.08
CH_4 Methane (3.5 mM)	105.0	CH_3OH	0.01	0.03	0.02	0.42
		HCOOH	0.02	0.02	0.03	0.08

[*]Ref. 16. [†]kcal mol^{-1}. N.D.: Not detected. Conditions: [catalyst] = 1.0 μM, [$Na_2S_2O_8$] = 5.0 mM, *T* = 323 K, and reaction time = 3 h. Product concentrations were determined by ^{1}H NMR spectroscopy using DSS as an internal standard. Any byproducts except those listed in the table were not detected.

Extended Data Table 2 | Summary of the product concentrations obtained from the oxidation of alcohol derivatives in a mixed solvent of D_2O/CD_3CN (95:5, v/v) using 1-OD_2, 2-OD_2, and 3-OD_2 as catalysts

Substrate	$BDE_{C\text{-}H}$[*,†]	Product	Catalyst			
			None	**1**-OD_2	**2**-OD_2	**3**-OD_2
			[Product] (mM)			
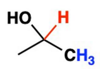	91.0 94.3	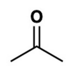	0.14	0.25	0.14	0.05
CH_3CH_2OH	94.6 101.3	CH_3COOH	0.08	0.18	0.12	0.03
CH_3OH	96.0	HCOOH	0.05	0.10	0.08	0.05

[*]Ref. 16. [†]kcal mol^{-1}. Conditions: [catalyst] = 1.0 μM, [$Na_2S_2O_8$] = 5.0 mM, [substrate] = 2.0 mM, *T* = 323 K, and reaction time = 3 h. Concentrations of products were determined by ^1H NMR spectroscopy using DSS as an internal standard. Any byproducts except those listed in the table were not detected.